Article

Flow-Induced Vibration of a Reversed U-Shaped Jumper Conveying Oil-Gas Two-Phase Flow

Hongjun Zhu [1,*](#), Tang Tang [1] and Quanhua Li [2]

1   State Key Laboratory of Oil and Gas Reservoir Geology and Exploitation, Southwest Petroleum University, Chengdu 610500, China
2   Shenzhen Branch, CNOOC Co., Ltd., Shenzhen 518000, China
*   Correspondence: ticky863@126.com

Abstract: Subsea jumpers connecting the underwater wellhead and nearby manifold commonly undergo flow-induced vibration (FIV) due to the spatially frequent alteration in the flow direction, velocity, pressure and phase volume fraction of the oil–gas two-phase flow, potentially leading to fatigue damage. This paper reports the numerical results of the FIV of a reversed U-shaped jumper excited by gas–liquid two-phase flow, which evolves from the initial slug flow with a fixed gas–liquid ratio of 1:2 when transporting through the jumper. The FIV response and flow pattern evolution are examined with a gas flow rate of Q_g = 4–12 kg/s and a liquid flow rate of Q_L = 96–288 kg/s. When the gas–liquid flow passes through the jumper, the flow regime subsequently presents the slug flow, bubble flow, churn flow and imperfect annular flow. The out-of-plane response frequency coincides with the pressure fluctuation frequency for the four connecting bends, suggesting the fluid–structure interaction (FSI). Nevertheless, the vibration displacement is limited with the maximum value less than 0.0014D (where D is the jumper diameter) in the present considered flow rate range.

Keywords: reversed U-shaped jumper; gas–liquid two-phase flow; flow pattern evolution; flow-induced vibration; fluid–structure interaction

1. Introduction

A subsea production system consists of seabed wellheads, production trees, subsea tie-ins, jumpers and control facilities [1,2]. Among them, subsea jumpers are pipe connectors used to transport oil and gas fluids between two subsea components (e.g., trees, manifolds or PLETs) [3]. Therefore, jumpers are designed to allow for expansion and contraction due to the pressure and thermal variations and the fabrication and installation tolerances. The common configurations for jumpers include Z shape, M shape, V shape and reversed U shape [4,5]. Due to the frequent alteration of the flow direction, the vibration response is easily excited, known as the flow-induced vibration (FIV), which is the main contributor to fatigue damage [6].

Since the response is induced by the internally transported flow, the flow regime and associated characteristics of the gas–liquid flow have been extensively investigated. Mandhane et al. [7] and Taitel et al. [8] conducted experimental studies on the flow pattern of the gas–liquid two-phase flow in both horizontal and vertical pipes, providing the typical flow pattern maps for the following works. Wallis [9], Shoham [10] and Liu et al. [11] theoretically examined the effects of the average velocity of the gas–liquid two-phase flow, droplet size and liquid film thickness on the flow evolution. Several models were proposed to predict the flow pattern and heat transfer coefficient. Ohnuki et al. [12] and Fan et al. [13] experimentally and numerically investigated the flow characteristics of gas–liquid fluids in vertical pipes, respectively. The results show that the flow pattern transition is closely related to the gas–liquid flow rate ratio, pipe diameter and the liquid and gas properties. Mohmmed et al. [14] carried out a one-way fluid–structure interaction (FSI) simulation of the gas–liquid slug flow in a horizontal pipe. It was found that the structural dynamic

response is associated with the slug formation and the induced stress acting on the pipe wall. In summary, although the flow regime of the gas–liquid mixture in vertical and horizontal pipes has been documented, the alteration of the two-phase flow in an oscillating pipe and its interaction with the pipe response are not well understood.

In contrast, the FIV of pipe bends is mainly attributed to the sudden momentum and pressure change when a two-phase flow passes through them [15]. Miwa et al. [16] theoretically studied the fluctuating force acting on a horizontal 90° pipe bend excited by gas–liquid two-phase flow. A model was built to predict the fluctuation frequency and the magnitude of the fluid force caused by stratified wavy flow. Liang et al. [17] analyzed the dynamic response of a 90° bend using the two-way FSI simulation. It was observed that the response displacement reduces with a decrease in the gas–liquid ratio. Laurent et al. [18] numerically investigated the two-phase flow in a U tube and found that the structure vibration is closely related to the damping coefficient.

Jumpers possess more than one bend. Elyyan et al. [19] used a 3-*D* simulation to numerically investigate the fluid–structure interaction (FSI) of an M-shaped jumper and estimated the deformation due to hydrodynamic fluctuations. It was found that the slug frequency is one of the main factors affecting the total fluid force and FIV response. For steady operation conditions, one-way FSI is sufficient to capture the maximum deformation and dominant frequency. In a similar vein, Li et al. [20] used the general finite element (FE) code ANSYS CFX and ANSYS Mechanical to carry out the FSI analysis of a jumper conveying gas–water two-phase flow with both ends fixed. It is reported that the mixture velocity, liquid and gas superficial velocities and slug frequency are the main factors determining the pipeline vibration [21,22]. Jia [23] numerically investigated the slug flow-induced vibration of a jumper and reported that the vibration amplitude was closely related to the flow rate, slug length and slug frequency. Chica et al. [24] used a combination of finite element analysis (FEA) and computational fluid dynamics (CFD) to numerically study the air–water two-phase flow-induced response of an M-shaped jumper. It was found that randomly developing slugs in the vertical section of the jumper excited a strong response when the slug frequency was close to the natural frequency.

Although the FIV of the M-shaped jumper has been studied by several scholars, the dynamic behavior and associated gas–liquid two-phase flow evolution in the oscillating jumper are far from well understood. Therefore, the FIV of an inverted U-shaped jumper excited by the gas–liquid two-phase flow that evolves from an initial slug flow was numerically investigated to reveal the intrinsic relationship between the vibration response and the gas–liquid flow evolution.

2. Problem Description

2.1. Basic Parameters

As shown in Figure 1, the jumper includes two vertical tubes and three horizontal tubes, which are connected by four bends of identical diameters. The length of the inlet horizontal tube is $L_1 = 40D$, to allow oil and gas to fully develop before entering the first bend, while the length of the outlet horizontal tube is $L_3 = 31.5D$. Both the two vertical tubes have a height of $H = 20D$ and are connected with a horizontal tube of length $L_2 = 20D$. The radius of the four bends is $R_0 = 4D$. The detailed parameters of the jumper are summarized in Table 1. The coordinate origin is defined at the inlet, the *x*-axis is along the flow direction of the inlet horizontal pipe section and the *z*-axis is along the direction of the vertical inlet pipe section, so it is arranged on the *XOZ* plane at the initial moment. Therefore, the oscillations along the *X* and *Z* directions are called the in-plane response, while the vibration along the *Y* direction is named the out-of-plane response. The cross-sections at the midspans of four bends (A-A, B-B, C-C and D-D) and three probes in the midspan of three key tubes (Probe 1, Probe 2 and Probe 3) are selected to monitor the fluctuations of the pressure and vibration displacement. Both ends of the jumper are fixed in the simulations to examine the vibration response.
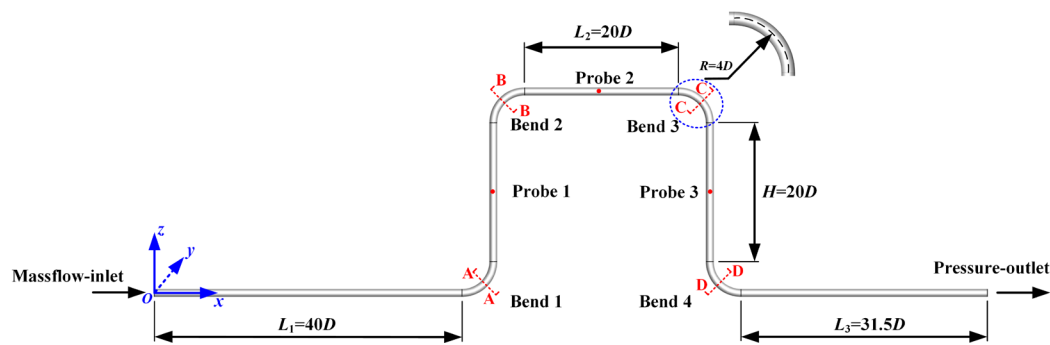
Figure 1. Schematic of the reversed U-shaped jumper with the geometric definition and boundary conditions, where A-A, B-B, C-C and D-D are the cross-sections at the midspans of four bends, and Probe 1, Probe 2 and Probe 3 are three probes in the midspan of three key tubes.

Table 1. Key parameters of the reversed U-shaped jumper.

Parameter	Value	Unit
Length of the upstream horizontal tube, L_1	10	m
Length of the top horizontal span, L_2	5	m
Length of each vertical tube, H	5	m
Length of the downstream horizontal tube, L_3	8	m
Internal diameter, d	0.211	m
External diameter, D	0.254	m
Curvature radius of each connecting bend, R/D	2	/
Young's modulus of the jumper, E	2.06	GPa
Poisson's ratio of the jumper, μ	0.321	/

The process of gas–liquid two-phase flow passing through the jumper at a back pressure of 6 MPa is numerically simulated [25]. Under this pressure, the associated densities of oil and natural gas are 960 kg/m^3 and 40.3 kg/m^3, respectively. The dynamic viscosities of oil and gas are 0.048 Pa·s and 1.09×10^{-5} Pa·s, respectively. In the simulations, the entire jumper is initially filled with oil. Then, the natural gas and oil are alternately injected into the inlet horizontal tube at a fixed time interval ratio of 1:2, which is accomplished by the user's defined function (UDF).

The frequency of the injected slug flow is defined as 1.67 Hz, i.e., the cycle $T = T_{\text{gas}} + T_{\text{oil}} = 0.6$ s. Considering the compressibility of natural gas, the inlet is set as a mass flow inlet, while the outlet is set as a pressure outlet with a pressure of 6 MPa. The gas mass flow rate ranges from 4 kg/s to 12 kg/s, accompanied by an increase in the liquid mass flow rate from 96 kg/s to 288 kg/s, ensuring a constant gas–liquid ratio of 1:2. The corresponding mixture velocity ranges from 2 m/s to 6 m/s, falling within the economically feasible flow rate range [8]. Figure 2 shows the time history of the pulsating gas–liquid two-phase flow, validating the generation of the slug flow, taking $Q_{m-in}^{G} = 6$ kg/s and $Q_{m-in}^{L} = 144$ kg/s as an example.

2.2. Modal Analysis

As illustrated in Figure 3, the modal analysis of the inverted U-shaped jumper is conducted using Ansys software to obtain the mode shape and natural frequency in two directions, namely, the in-plane XOZ and out-of-plane YOZ, in order to assess the fluid–structure interaction risk. The analysis reveals that the in-plane natural frequency (f_{x1} and f_{z1}) is approximately twice that of the out-of-plane natural frequency (f_{y1}). This finding is significant as it provides insights into the dynamic behavior of the jumper in response to the fluid–structure interaction.
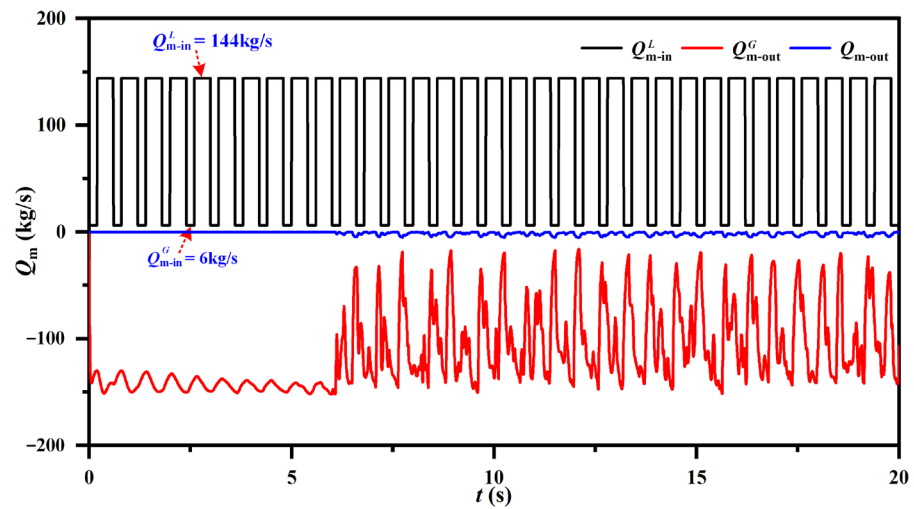
Figure 2. The monitored mass flow rates (Q_m) in both the inlet and outlet, here taking Q_{m-in}^{G} = 6 kg/s and Q_{m-in}^{L} = 144 kg/s for instance, where $Q_{m\text{-}in}$ and $Q_{m\text{-}out}$ represent the mass flow rate in the inlet and outlet boundaries, respectively, and superscript *L* and *G* denote the liquid and gas, respectively.
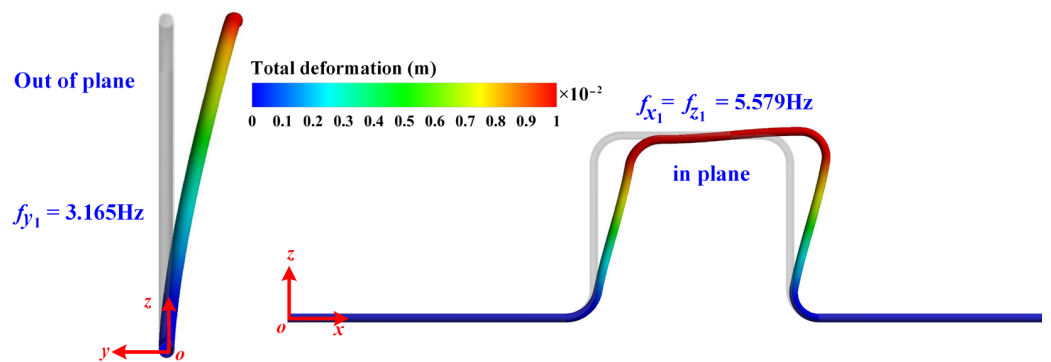

Figure 3. The fundamental modal shapes in both in-plane and out-of-plane directions obtained via modal analysis, where f_{x1}, f_{z1} and f_{y1} denote the fundamental natural frequencies in x, z and y directions, respectively.

3. Numerical Methods

3.1. Volume of Fluid Model

The volume of fluid (VOF) model is widely used to study gas–liquid two-phase flow [26–29]. This method, first introduced by Hirt and Nichols [30], is utilized to capture the gas–liquid interface. In this model, a single set of momentum equations is shared by the gas–liquid two phases, and the tracking of the interface between the gas and liquid is accomplished by the solution of a continuity equation [31,32]. The continuity and momentum equations used in the VOF model are given below [33,34]:

$$\frac{\partial \rho_m}{\partial t} + \frac{\partial \rho_m \overline{v_i}}{\partial x_i} = 0 \tag{1}$$

$$\frac{\partial \rho_m \overline{v_i}}{\partial t} + \frac{\partial \rho_m \overline{v_i}\overline{v_j}}{\partial x_j} = \rho_m g_i - \frac{\partial \overline{p}}{\partial x_i} + \mu_m \nabla^2 \overline{v_i} - \frac{\partial \rho_m \overline{v_i' v_j'}}{\partial x_j} + f_i \tag{2}$$

in which

$$\rho_m = \alpha \rho_G + (1 - \alpha)\rho_L \tag{3}$$

$$\mu_m = \alpha \mu_G + (1 - \alpha)\mu_L \tag{4}$$

where ρ_m and μ_m are the density and dynamic viscosity of the gas–liquid mixture, respectively; ρ_G and ρ_o are the gas density and oil density, respectively; μ_G and μ_L are the associated dynamic viscosities of the gas and oil; α is the gas void fraction; t is the flow time; x_i is the space coordinate in the i direction; v_i represents the instantaneous velocity component in the i direction. For example, v_1, v_2 and v_3 are the velocities in the X, Y and Z directions, respectively, while v_i' is the fluctuation velocity component in the i direction; g_i is the gravitational acceleration in the i direction; p is the pressure; f_i is the surface tension force between the phases in the i direction; and "$^-$" denotes the time-averaged value of the associated parameter.

The two-phase interface is meanwhile tracked by solving the gas phase volume fraction continuity equation [35]. It is assumed that there is no phase transition at the interface and no slip between the gas and liquid.

$$\frac{\partial \alpha}{\partial t} + \frac{\partial \alpha \overline{v_i}}{\partial x_i} = 0 \tag{5}$$

The RNG (renormalization group) *k*-epsilon (*k*-ε) turbulence model is employed to close the above equations. The turbulent kinetic energy (k) and its dissipation rate (ε) are given by:

$$\frac{\partial k}{\partial t} + \frac{\partial k \overline{v_j}}{\partial x_j} = \frac{\partial}{\partial x_j} \left[\left(\mu_m + \frac{\mu_t}{\sigma_k} \right) \frac{\partial k}{\partial x_j} \right] - \frac{\partial v_i \overline{v_i' v_j'}}{\partial x_j} - \varepsilon \tag{6}$$

$$\frac{\partial \varepsilon}{\partial t} + \frac{\partial \varepsilon \overline{v_j}}{\partial x_j} = \frac{\partial}{\partial x_j} \left[\left(\mu_m + \frac{\mu_t}{\sigma_\varepsilon} \right) \frac{\partial \varepsilon}{\partial x_j} \right] - C_{\varepsilon 1} \frac{\varepsilon}{k} \frac{\partial v_i \overline{v_i' v_j'}}{\partial x_j} - C_{\varepsilon 2} \frac{\varepsilon^2}{k} - R_\varepsilon \tag{7}$$

in which

$$\mu_t = C_\mu \rho_m k^2 / \varepsilon \tag{8}$$

$$R_\varepsilon = \frac{C_\mu \eta^3 (1 - \eta / \eta_0) \varepsilon^2}{(1 + \beta_0 \eta^3) k} \tag{9}$$

$$\eta = \frac{k}{\varepsilon} \left[\left(\frac{\partial v_i}{\partial x_j} + \frac{\partial v_j}{\partial x_i} \right) \frac{\partial v_i}{\partial x_j} \right]^{1/2} \tag{10}$$

where μ_t is the turbulent viscosity; R_ε is an extra strain rate term; and the constants are set as $C_\mu = 0.1$, $C_{\varepsilon 1} = 1.44$, $C_{\varepsilon 2} = 1.92$, $\sigma_k = 1.0$, $\sigma_\varepsilon = 1.3$, $\eta_0 = 4.38$ and $\beta_0 = 0.012$, respectively [36]. The above equations are solved using the finite volume method (FVM) coupled with the pressure-implicit with splitting of operators (PISO) algorithm. The first-order implicit scheme and the second-order inverse upwind scheme are used for the temporal discretization and the spatial discretization of convective terms [37].

The vibration response of the jumper is solved by [38]:

$$[M_S]\left\{\ddot{U}\right\} + [K_S]\{U\} = [F_S] + [R]\{P\} \tag{11}$$

$$\begin{bmatrix} M_S & 0 \\ \rho R^T & M_f \end{bmatrix} \left\{ \begin{array}{c} \ddot{U} \\ \ddot{P} \end{array} \right\} + \begin{bmatrix} K_s & -R \\ 0 & K_f \end{bmatrix} \left\{ \begin{array}{c} U \\ P \end{array} \right\} = \left\{ \begin{array}{c} F_S \\ F_f \end{array} \right\} \tag{12}$$

where P is the pressure; 'K' is the stiffness matrix with the subscripts '*s*' and '*f*' defining a solid and fluid, respectively; $[M_s]$ and $[M_f]$ are the mass matrix for a solid and fluid, respectively; $[F_s]$ and $[F_f]$ are the force matrix for a solid and fluid, respectively; and $[R]$ is a coupling matrix. In the simulation, the time-step Δt is set as 0.005 s to ensure the Courant number is below 1.0.

In the two-way fluid–structure interaction (FSI) iteration, the above governing equations of the flow field (Equations (1)–(5)) and structure motion (Equations (11) and (12)) are solved alternately. The multi-field solver of the ANSYS MFX software package is utilized to

conduct the two-way FSI calculation, which is performed until satisfactory periodic results are obtained [39].

3.2. Meshing and Dependence Check

The fluid and solid domains depicted in Figure 4 were discretized using structured grids, with refined grids near the bends and jumper surfaces. The height of the first grid layer was set as 0.0098D to ensure a normalized wall distance $y^+ \leq 10$. A mesh independence check was conducted by varying the number of grid units in the radial and axial directions of the computational domain. As listed in Table 2, an increase in the grid number results in a smaller numerical discrepancy. The resolution of Mesh-4 (with a total of 1,034,924 grids) is finally selected for the numerical simulations.
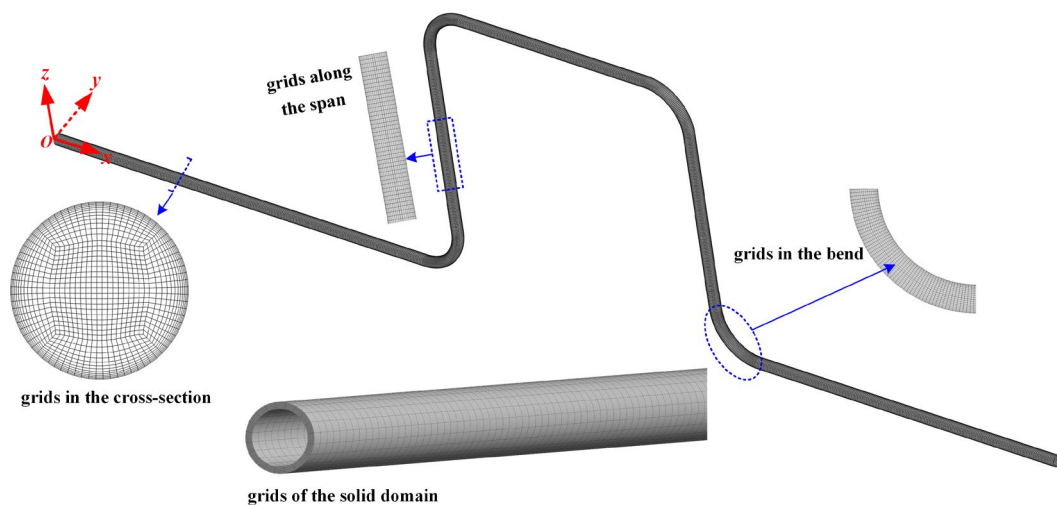
Figure 4. Computational mesh of both fluid and solid domains.

Table 2. Mesh independence check.

No.	Elements	Pressure Acting on Bend 1 (KPa)	Pressure Acting on Bend 2 (KPa)	Pressure Acting on Bend 3 (KPa)	Pressure Acting on Bend 4 (KPa)
M1	328,416	95.84	74.27	60.89	40.92
M2	492,624	108.58(13.29%)	83.95 (13.03%)	68.78 (12.96%)	46.28 (13.10%)
M3	662,836	118.86 (9.47%)	92.16 (9.78%)	75.56 (9.86%)	50.52 (9.16%)
M4	821.059	125.21 (5.34%)	97.15 (5.41%)	79.55 (5.28%)	53.15 (5.21%)
M5	1034.924	126.49 (1.03%)	98.15 (1.03%)	80.35 (1.01%)	33.72 (1.07%)

3.3. Numerical Validation

Based on the experimental results of Mandhane [7] and Taitel [8], different flow patterns in horizontal and vertical pipes, respectively, were validated using the present numerical method. As shown in Figure 5, the diameter and length of the vertical pipe are 1 in and 3 m, respectively. The diameter and length of the horizontal pipe are 1 in and 3.25 m, respectively. The numerical results demonstrate that five flow patterns of stratified flow (v_G = 0.9 m/s, v_L = 0.6 m/s), bubble flow (v_G = 0.3 m/s, v_L = 1.2 m/s), slug flow (v_G = 5 m/s, v_L = 2 m/s), wavy flow (v_G = 12 m/s, v_L = 0.3 m/s) and annular flow (v_G = 101 m/s, v_L = 0.8 m/s) fall into the flow regime map proposed by Mandhane [7] for a horizontal pipe. Similarly, four flow patterns of bubble flow (v_G = 0.87 m/s, v_L = 3.9 m/s), churn flow (v_G = 0.2 m/s, v_L = 0.5 m/s), slug flow (v_G = 1.4 m/s, v_L = 0.15 m/s) and annular flow (v_G = 10.35 m/s, v_L = 0.3 m/s) coincide well with the flow regime partition reported by Taitel [8] for a vertical pipe.
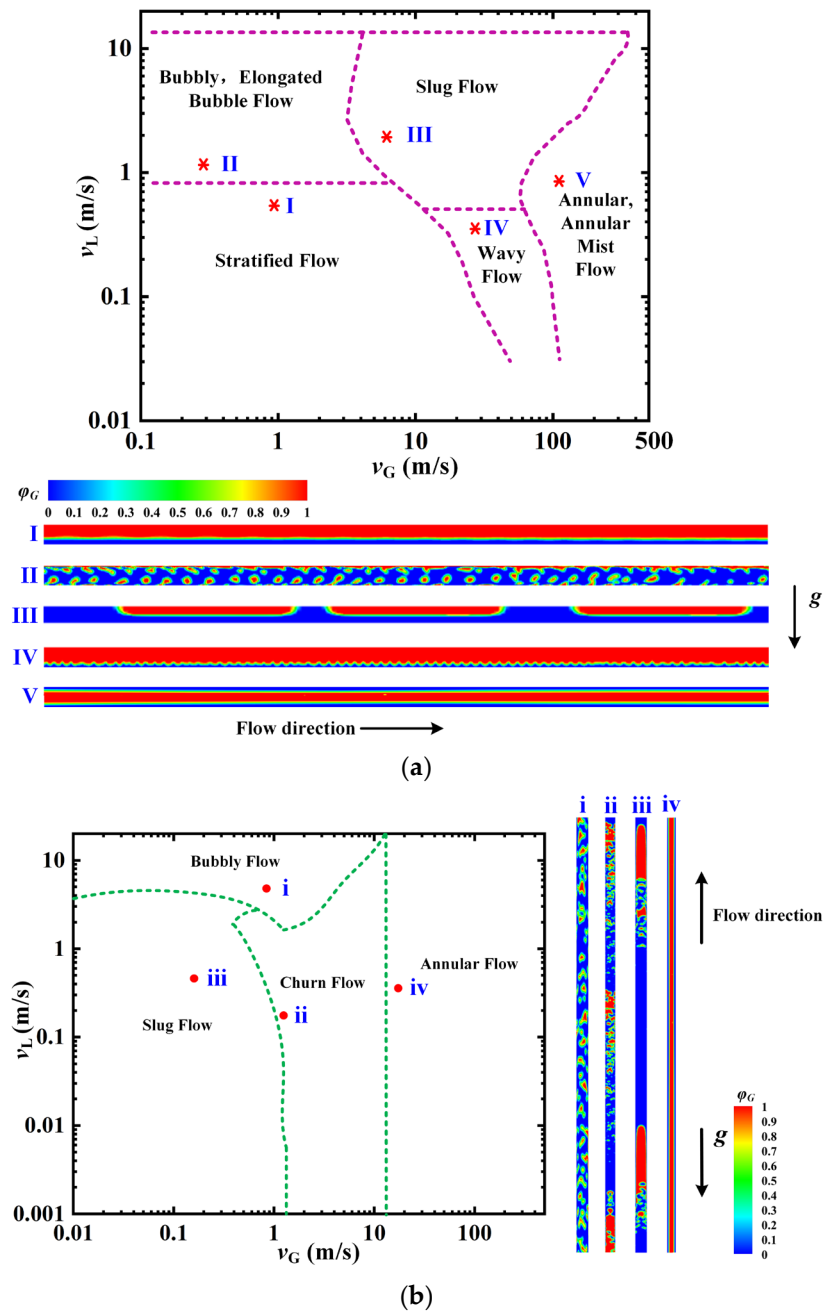
Figure 5. Model validation for the production of gas–liquid two-phase flow regimes in both horizontal and vertical tubes against the reported flow pattern maps, where v_G and v_L are the gas and liquid superficial velocities, respectively: (**a**) flow regimes in a horizontal tube [7], where the red stars denote the simulated cases; (**b**) flow regimes in a vertical tube [8], where the red circles denote the simulated cases.

Figure 6 shows a comparison of the experimental and numerical results of air–water two-phase flow in an inverted U-shaped jumper [40]. The internal and external diameters of the test pipe are 1 in and 1.3 in, respectively. The length and height of the U-bend are 1.24 m and 0.3 m, respectively. The radius-to-diameter ratio (R/D) is 0.4. The flow pattern evolution of the slug flow in the pipe is presented in Figure 6a for a duration of time with $v_{air} = 0.51$ m/s and $v_{water} = 0.46$ m/s. In addition, Figure 6b displays the root-mean-squared vibration amplitudes in different directions. Both the flow regimes and the vibration amplitudes show a good agreement, suggesting the applicability of the current numerical method.
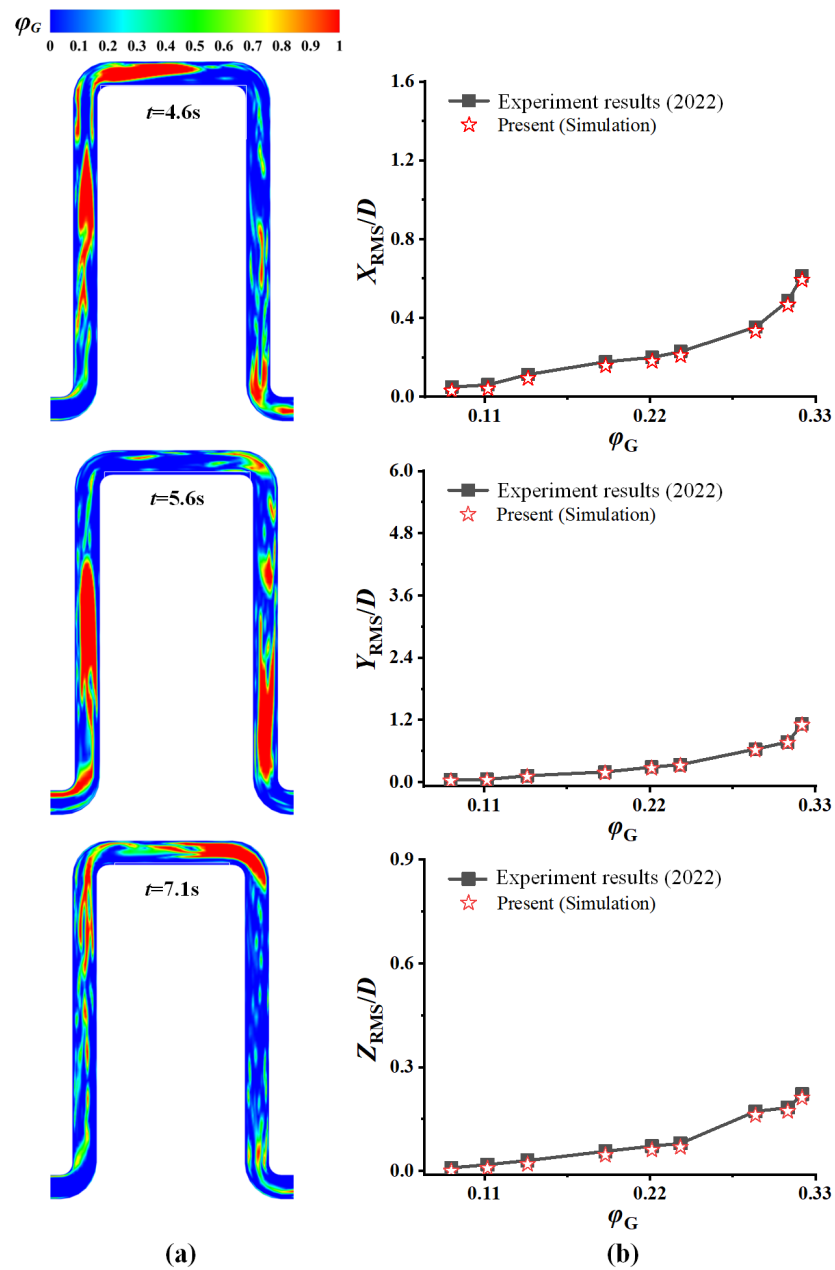
Figure 6. Model validation for the vibration response of a reversed U-shaped tube against the experimental results reported by Bamidele et al. [40]: (**a**) comparison of the flow pattern morphology between the present CFD simulation and the experiment at v_{air} = 0.51 m/s and v_{water} = 0.46 m/s; (**b**) the root-mean-squared displacements of the upper right bend in three directions.

4. Results and Discussion

4.1. Flow Characteristics

4.1.1. The Pressure Variation at Bends

In transportation pipelines, the pressure drop is an important parameter for evaluating energy loss [41]. Figure 7 presents the time histories of the pressure acting on the four bends and their associated wave-let frequency spectra in the case of Q^G_{m-in} = 6 kg/s and Q^L_{m-in} = 144 kg/s. Although the pressure decreases as the flow passes through the jumper, the total pressure follows the same trend. The pressure in Bend 2 and Bend 4 drops sharply due to the friction loss and the alteration of the static head [42]. The wave-let frequency reveals that the same dominant frequency f_1 of the pressure fluctuation at the four bends is consistent with the slug frequency of 1.67 Hz, while the secondary frequency of 3.34 Hz is

possibly caused by the unstable flow evolution. The secondary frequency of the pressure fluctuation is roughly double the dominant one, signifying a harmonic frequency.
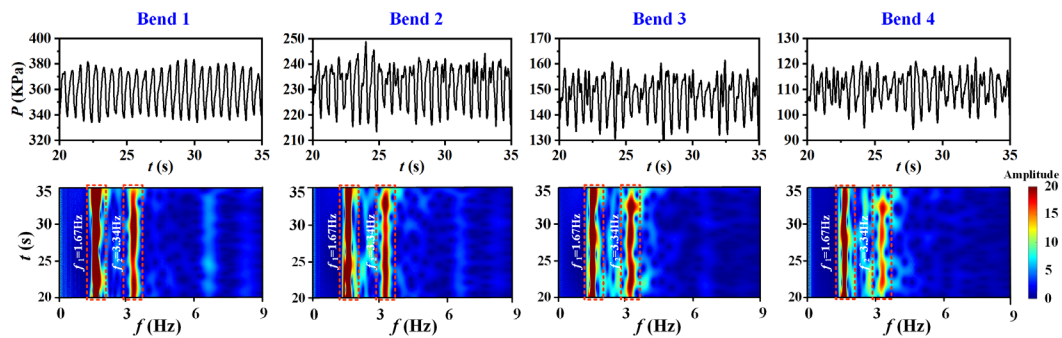

Figure 7. Time histories of the pressure acting on four bends and associated wave-let frequency spectra in the case of Q^G_{m-in} = 6 kg/s and Q^L_{m-in} = 144 kg/s.

4.1.2. Flow Pattern Evolution

Figure 8 shows the changes in the flow pattern when the gas–liquid flow passes through Bend 2. The flow rates of the gas and liquid are Q^G_{m-in} = 6 kg/s and Q^G_{m-in} = 144 kg/s, respectively. Eight representative moments are denoted as t_1–t_8. When the slug flow enters the bend, it is difficult for the gas plug to maintain the original shape. Instead, large gas bubbles are observed in the bend, due possibly to the existence of centrifugal force. After that, the gas bubbles regather and form an elongated large bubble in the horizontal midspan tube. Meanwhile, Bend 2 presents the annular flow regime until the next gas plug arrives.
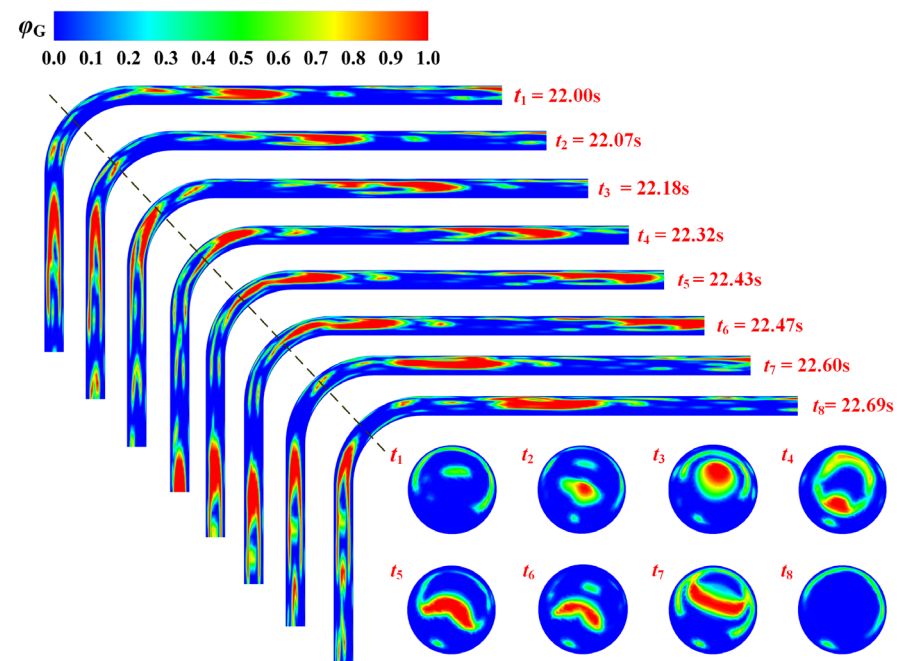

Figure 8. The evolution of gas–liquid two-phase flow through Bend 2 and the associated gas volume fraction in the B-B cross-section in the case of Q^G_{m-in} = 6 kg/s and Q^L_{m-in} = 144 kg/s, where t_1–t_8 denotes eight representative moments.

Figure 9 shows the evolution of a gas plug passing throughout the whole jumper. When the gas–liquid reaches the first bend (Bend 1), the gas (methane) moves faster than the liquid (oil) due to the buoyancy, resulting in the stretching of the gas plug in the subsequent upward tube. Additionally, Bend 1 presents a stratified flow. Subsequently, the vertical upward pipe presents the churn flow. Due to the participation of centrifugal force, the

gas plug is squeezed at the second bend (Bend 2). Then, the gas gathers at the top of the horizontal span in the form of an elongated bubble due to buoyancy. At Bend 3, the gas and liquid flow along the extrados and intrados, respectively, exhibiting a stratified flow regime. Subsequently, due to the inertial force, the gas–liquid two-phase flow descends rapidly in the vertical downward pipe, generating an irregular annular flow. After that, the gas accumulates at the top of the last horizontal tube, and the two-phase flow eventually exits the jumper in the form of the bubbly regime.
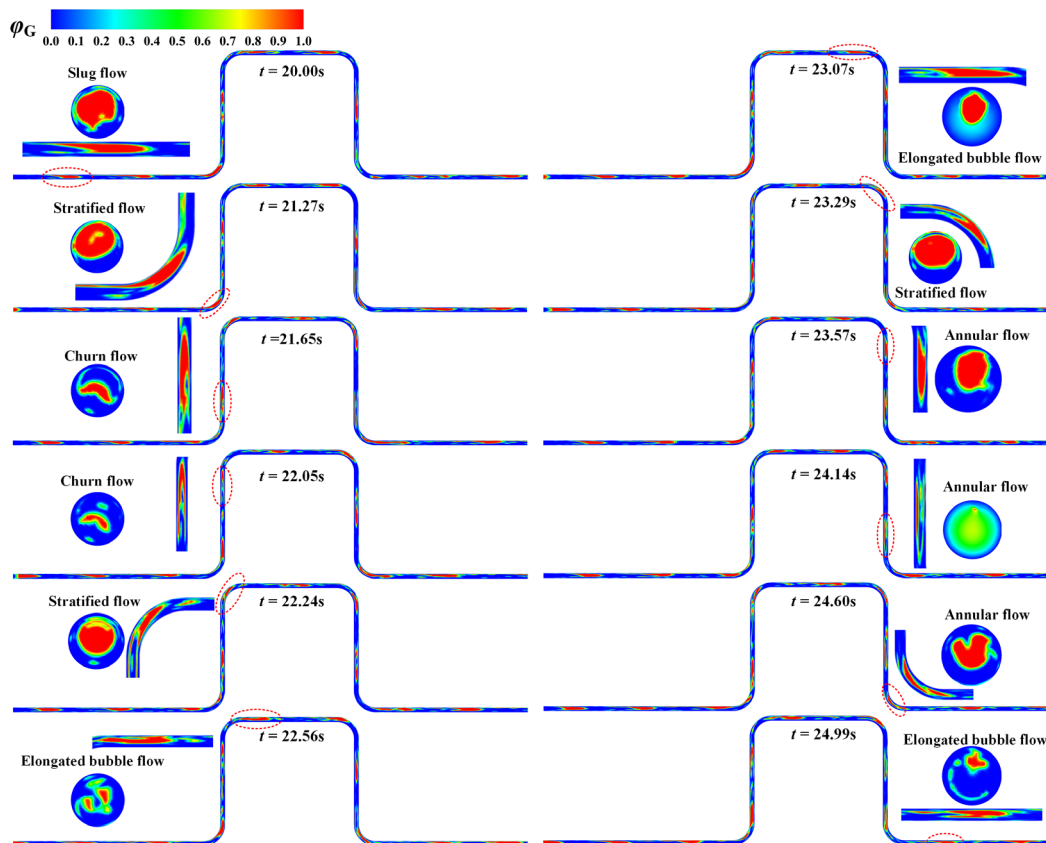
Figure 9. Spatial evolution of a gas plug that is injected from the inlet passing through the jumper in the case of Q_{m-in}^{G} = 6 kg/s and Q_{m-in}^{L} = 144 kg/s.

4.2. Vibration Response

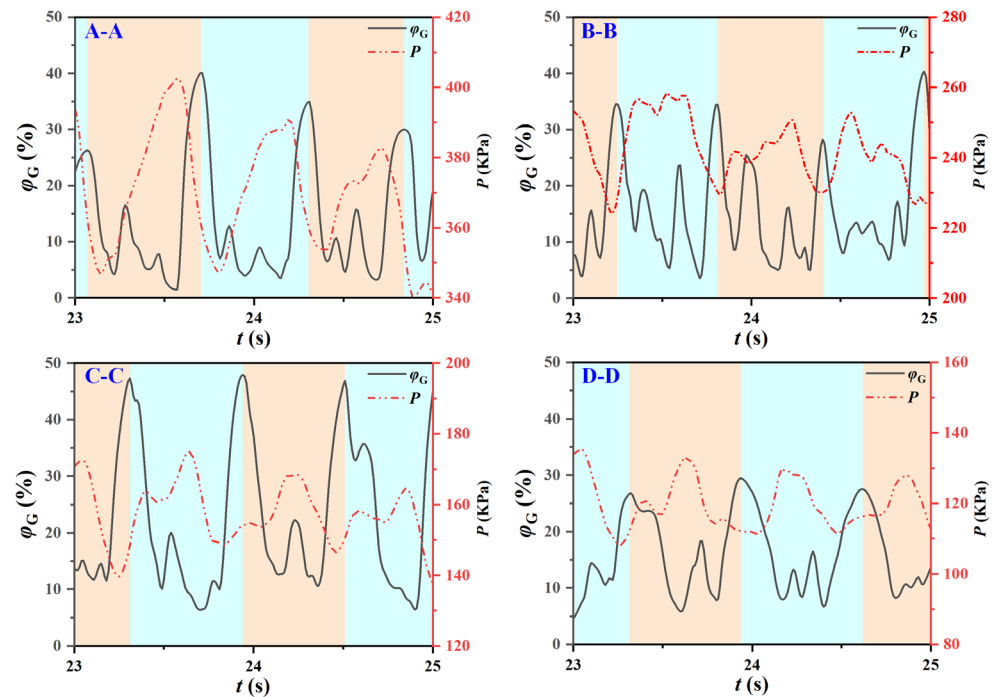Figure 10 depicts the variations of the pressure and gas volume fraction in the middle cross-sections of the four bends in the case of Q_{m-in}^{G} = 6 kg/s and Q_{m-in}^{G} = 144 kg/s. Among the four sections, the highest pressure is observed in section A-A, whereas section D-D experiences the lowest pressure, illustrating the energy loss along the jumper Sections B-B and C-C exhibit a minimal difference because they are situated on the same horizontal plane with relatively low energy dissipation. The gas volume fraction presents a similar change in the four sections. The gas volume fraction in section C-C is the largest one due to the gas accumulation at Bend 3. In contrast, the gas volume fraction at section D-D drops significantly due to the gravity-driven dissipation in the vertical downward pipe. It is noted that the gas volume fraction generally fluctuates in the antiphase with that of pressure, signifying the larger pressure is mainly contributed from the liquid phase.

Figure 11 shows the time histories of the vibration displacements of the four bends and three probes, along with the corresponding time-averaged and root-mean-squared values in the case of Q_{m-in}^{G} = 6 kg/s and Q_{m-in}^{G} = 144 kg/s. The vibration displacements (Y/D) of Bend 1 and Bend 4 are smaller than those of Bend 2 and Bend 3 due to the influence of the adjacent fixed ends of the jumper. As a result of the spatial configuration, Bend 1 undergoes a positive horizontal oscillation, whereas Bend 4 presents a negative one. In

contrast, the vertical displacements (Z/D) of Bend 1 and Bend 4 are relatively large, due possibly to the alteration of the flow direction between the horizontal and vertical. Both the in-plane and out-of-plane displacements of Probe 1 and Probe 3 are smaller than those of Probe 2, suggesting the occurrence of the greatest response at the midspan. The spatial displacements generally present a symmetric distribution, where the midspan (Probe 2) exhibits the largest time-averaged and root-mean-squared (RMS) values, followed by Bend 2 and Bend 3.

Figure 10. Fluctuations of the pressure and gas volume fraction in the middle cross-sections of the four bends in the case of Q_{m-in}^G = 6 kg/s and Q_{m-in}^L = 144 kg/s.

Figure 12 presents the time-varying response profiles (solid lines) and the associated RMS displacement profile (dashed line) of the rigid jumper in the case of Q_{m-in}^G = 6 kg/s and Q_{m-in}^G = 144 kg/s. The profile of RMS displacement suggests the fundamental mode dominates the X- and Y-directional responses. The greatest vibration occurs in the horizontal direction (X), followed by the out-of-plane (Y). As illustrated in Figure 13, the vibration energy is primarily concentrated at the position where the amplitude reaches the peak value [43]. It is clearly seen that the energy is concentrated at the midspan for the X- and Y-directional responses, further demonstrating that the first-order vibration dominates the vibration. Due to the flow evolution in the jumper, multiple frequencies take part in the in-plane response.

4.3. Effect of Inflow Mass Flow Rate

The pressure fluctuations of the four bends and their frequency spectra at different inlet mass flow rates are compared in Figure 14. The results show that, for a given bend, the pressure acting on the bend increases with the inlet mass flow rate due to the increase in the momentum flux. The dominant fluctuation frequencies of pressure are consistent with the inlet slug frequency, which is approximately half of the out-of-plane fundamental natural frequency, indicating that the pressure variation depends on the flow pattern.

Figure 15 displays the root-mean-squared displacements and new equilibrium positions at various inlet mass flow rates, which are denoted by the mixture velocities (v_{mix}). The RMS amplitudes in the jumper plane increase with the inlet mass flow rate, while the out-of-plane RMS amplitude increases first and then decreases. The in-plane new equilibrium position indicates that the rigid jumper experiences a certain axial deformation

and attains a new equilibrium position when subjected to stress. The axial deformation gradually increases with the inlet mass flow rate, as evidenced by the clear displacements of Bend 2 and Bend 3.
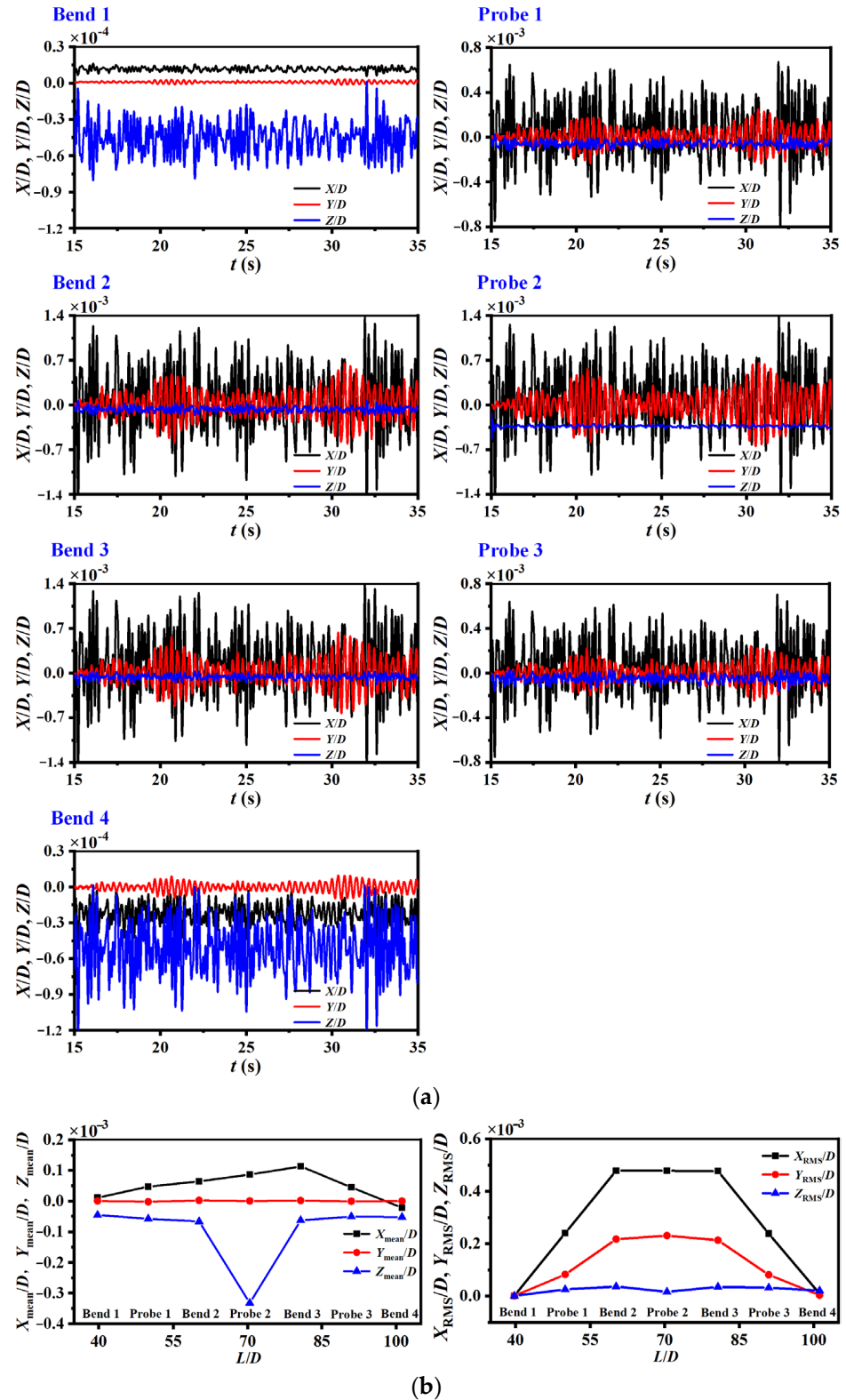

(a)

(b)

Figure 11. Vibration response in the case of Q_{m-in}^G = 6 kg/s and Q_{m-in}^L = 144 kg/s: (**a**) time histories of the response displacements of the four bends and three probes; (**b**) the associated time-averaged and root-mean-squared values.
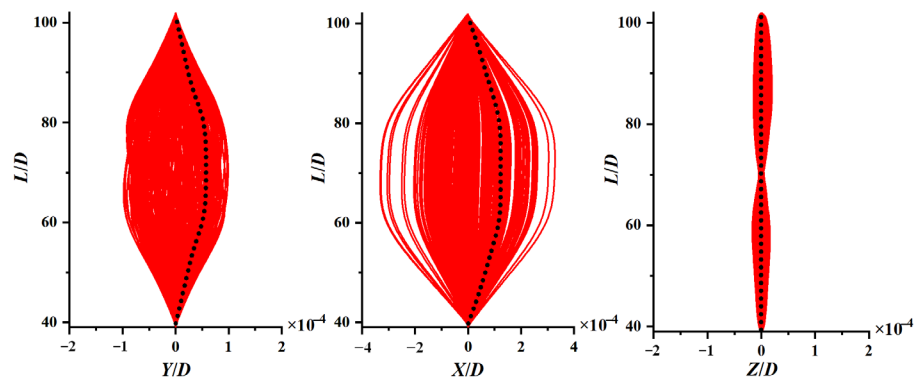
Figure 12. The time-varying response profiles (solid lines) and associated RMS displacement profiles (dashed lines) along the three directions in the case of $Q_{m-in}^{G} = 6$ kg/s and $Q_{m-in}^{L} = 144$ kg/s.
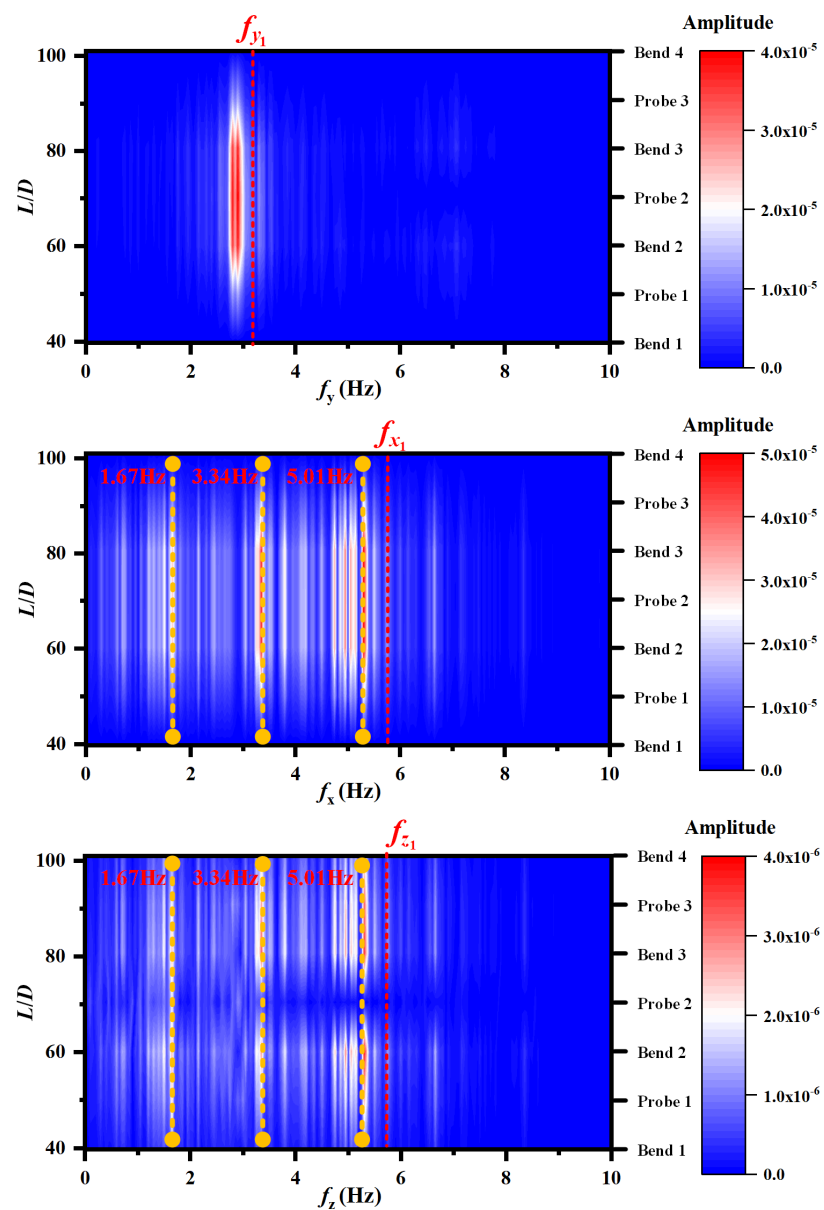
Figure 13. The spatial evolution of response frequencies along the jumper span in the case of $Q_{m-in}^{G} = 6$ kg/s and $Q_{m-in}^{L} = 144$ kg/s.

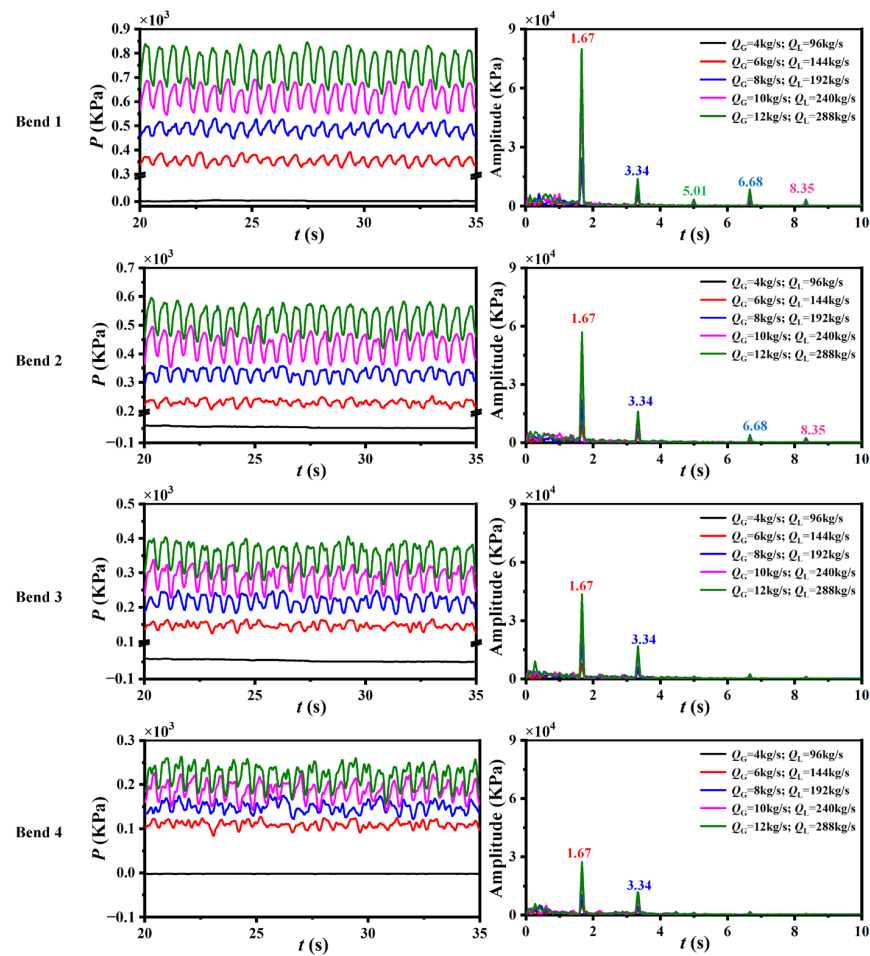**Figure 14.** Time histories of the pressure acting on the four bends and associated frequency spectra at different inlet mass flow rates.
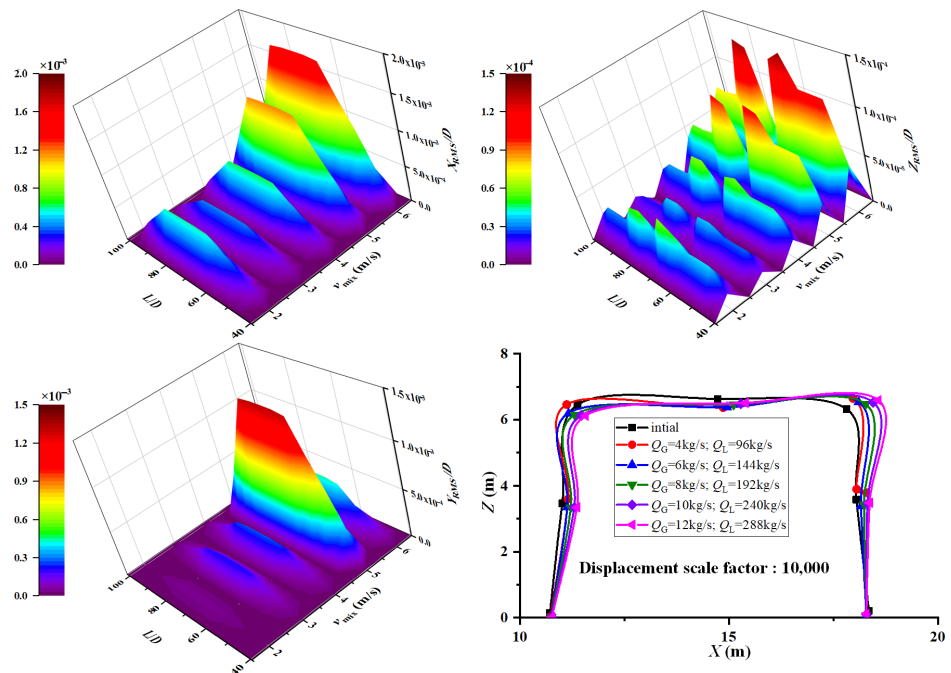

Figure 15. The root-mean-squared displacements along the jumper span and the new equilibrium positions in the in-plane at different inlet mass flow rates.

Figure 16 depicts a comparison of the gas plug length generated in the upstream horizontal tube and the flow evolution in the first bend (Bend 1) at various inlet mass flow rates. The gas–liquid two-phase flow evolves from the stable slug to the bubbly or churn regime when it passes through Bend 1. The number of gas plugs observed in the horizontal pipe decreases with an increase in the flow rate, while the average length of the gas plug gradually increases. Figure 17 compares the instantaneous snapshots of the flow regimes in the jumper at varying inlet mass flow rates. It is seen that the flow evolution is similar for the considered cases. By increasing the inlet mass flow rate, the gas bubble in the middle horizontal tube is elongated. When the gas–liquid fluid flows into the vertically downward pipe, the increased momentum contributes to the flow evolution from the bubbly to imperfect annular flow regime.
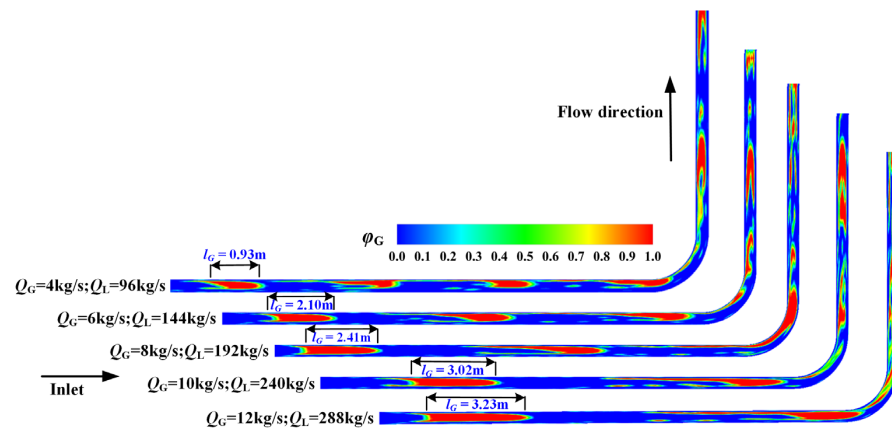

Figure 16. Comparison of the gas plug length produced in the upstream horizontal tube and the flow evolution in the first bend (Bend 1) at different inlet mass flow rates.
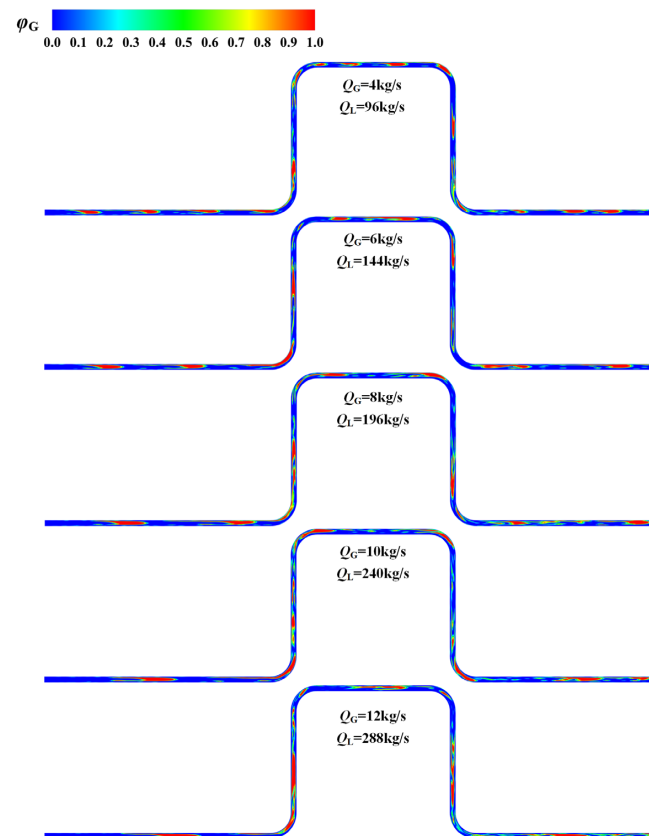

Figure 17. Comparison of the flow regimes (instantaneous snapshots after the flow reaches periodic stability) in the jumper at different inlet mass flow rates.

Figure 18 provides the temporal–spatial evolution of the response displacements and the associated spatial variation of the response frequencies at different inlet mass flow rates. The out-of-plane vibration frequency is close to the fundamental natural one, increasing slightly with the inlet mass flow rate. Accordingly, the out-of-plane displacement increases. The same trend is observed in the X direction, where the vibration frequency is consistent with the slug frequency. In contrast, for the Z direction, the vibration involves a staggered back-and-forth motion between the two ends due to the specific reversed U-shaped configuration.
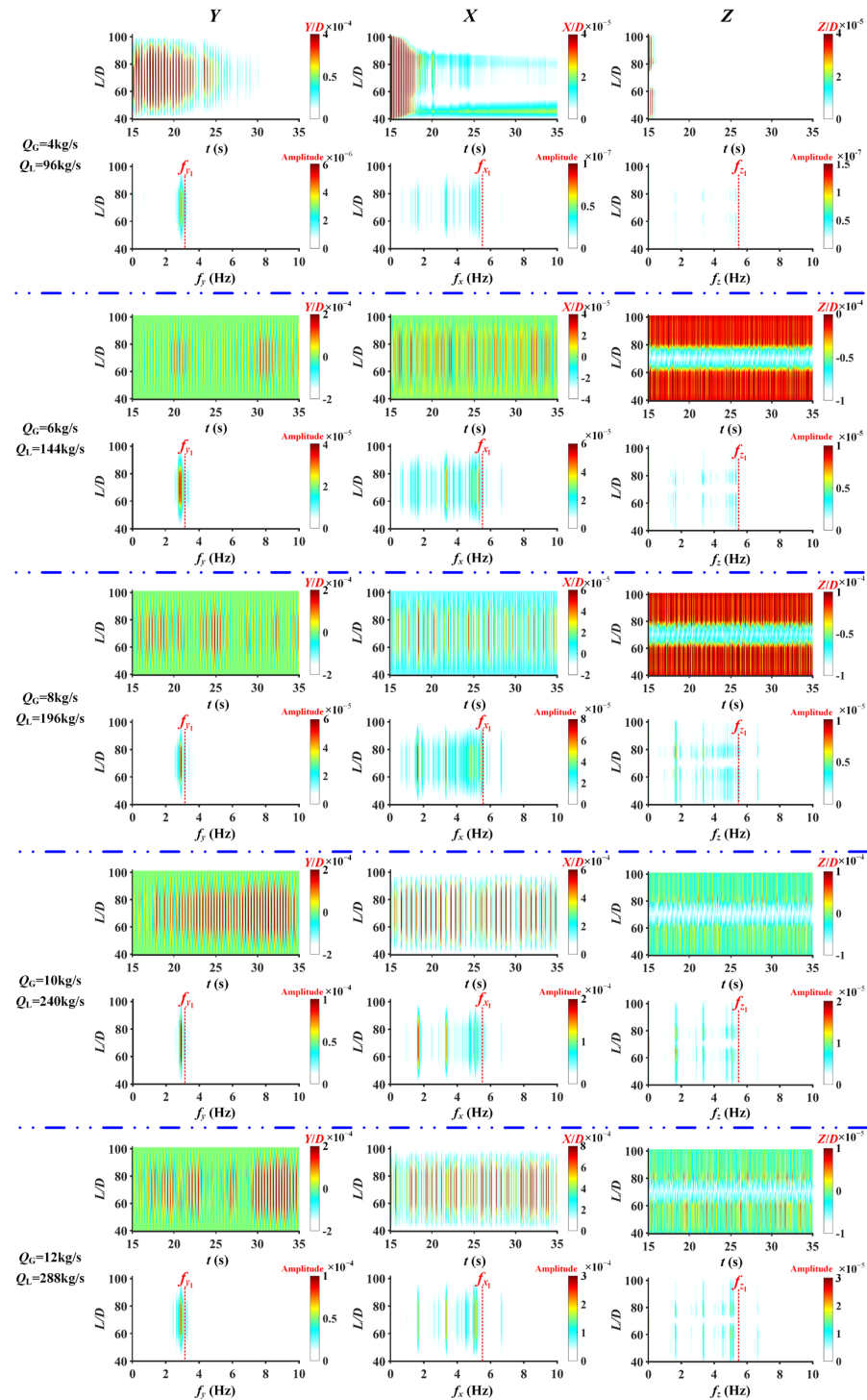

Figure 18. The temporal–spatial evolution of response displacements and the associated spatial variation of response frequencies at different inlet mass flow rates.

5. Conclusions

This study reports the flow behavior of gas–liquid two-phase flow in a reversed U-shaped subsea jumper and the resultant response. Based on the numerical results, several conclusions are drawn:

(1) The gas–liquid flow is predominantly characterized by the slug regime in horizontal tubes and the bubbly or churn regime in vertical tubes. The fluid force exerted on the first bend is found to be the largest, resulting in the highest vibration response amplitude. Furthermore, the vibration dominant frequency of the jumper is consistent with the slug frequency.

(2) With an increase in the mass flow rate, the fluid force pulsation amplitude acting on each bend increases, resulting in a corresponding increase in the response amplitude. Additionally, the average length of the gas plugs passing through the middle horizontal span also increases. The vibration of the jumper is dominated by the fundamental mode, with the vibration frequency being consistent with the pressure fluctuation frequency.

(3) The vibration displacement of the rigid jumper is found to be minimal, with the maximum displacement occurring at a position of only $0.0014D$. Moreover, the vibration response of the bend is dominated by the fundamental mode although the mass flow rate of the gas–liquid two-phase is increased.

In summary, the present numerical study predicts the vibration response and flow pattern evolution of gas–liquid two-phase flow in a subsea jumper. Further investigation is required to reveal the coupling response of a jumper under the combination effect of internal and external flows.

Author Contributions: Conceptualization, H.Z.; methodology, H.Z.; software, H.Z.; validation, T.T.; formal analysis, T.T.; investigation, T.T.; writing—original draft preparation, H.Z.; writing—review and editing, T.T. and Q.L.; visualization, T.T.; supervision, H.Z.; funding acquisition, H.Z. All authors have read and agreed to the published version of the manuscript.

Data Availability Statement: Not applicable.

Conflicts of Interest: The authors declare no conflict of interest.

References

1. Bai, Y.; Bai, Q. *Subsea Engineering Handbook*; Gulf Professional Publishing: Houston, TX, USA, 2018.
2. Sotoodeh, K. A review on subsea process and valve technology. *Mar. Syst. Ocean. Technol.* **2019**, *14*, 210–219. [CrossRef]
3. Toleman, B.; Huang, C.; Sonawane, M.; Shankaran, R.; Foster, D. Subsea Rigid Jumper Design Optimization for Sour Service Application. In Proceedings of the ASME 2019 38th International Conference on Ocean, Offshore and Arctic Engineering, Glasgow, UK, 9–14 June 2019.
4. Li, W.; Zhou, Q.; Yin, G.; Ong, M.C.; Li, G.; Han, F. Experimental Investigation and Numerical Modeling of Two-Phase Flow Development and Flow-Induced Vibration of a Multi-Plane Subsea Jumper. *J. Mar. Sci. Eng.* **2022**, *10*, 1334. [CrossRef]
5. Song, G.B.; Zhang, P.; Li, L.Y.; Singla, M. Vibration control of a pipeline structure using pounding tuned mass damper. *J. Eng. Mech.* **2016**, *142*, 04016031. [CrossRef]
6. Kim, J.; Srinil, N. 3-*D* numerical simulations of subsea jumper transporting intermittent slug flows. In Proceedings of the International Conference on Offshore Mechanics and Arctic Engineering, American Society of Mechanical Engineers, Madrid, Spain, 17–22 June 2018.
7. Mandhane, J.M.; Gregory, G.A.; Aziz, K.A. Flow pattern map for gas-liquid flow in horizontal pipes. *Int. J. Multiphas. Flow.* **1974**, *1*, 537–553. [CrossRef]
8. Taitel, Y.; Dukler, A.E. A model for predicting flow regime transitions in horizontal and near horizontal gas-liquid flow. *AIChE J.* **1976**, *22*, 47–55. [CrossRef]

9. Wallis, G.B. *One-Dimensional Two Phase Flow*; Courier Dover Publications: Mineola, NY, USA, 2020. [CrossRef]
10. Shoham, O. *Mechanistic Modeling of Gas-Liquid Two-Phase Flow in Pipes*; Society of Petroleum Engineers: London, UK, 2006. [CrossRef]
11. Liu, Y.; Tong, A.; Ozbayoglu, E. An improved drift-flux correlation for gas-liquid two-phase flow in horizontal and vertical upward inclined wells. *J. Petrol. Sci. Eng.* **2020**, *195*, 107881. [CrossRef]
12. Ohnuki, A.; Akimoto, H. Experimental study on transition of flow pattern and phase distribution in upward air–water two-phase flow along a large vertical pipe. *Int. J. Multiphas. Flow.* **2000**, *26*, 367–386. [CrossRef]
13. Fan, J.; Zhang, X.; Cheng, L. Numerical simulation and experimental study of two-phase flow in a vertical pipe. *Aerosol. Sci. Technol.* **1997**, *27*, 281–292. [CrossRef]
14. Mohmmed, A.O.; Al-Kayiem, H.H.; Osman, A.B.; Sabir, O. One-Way Coupled Fluid–Structure Interaction of Gas-Liquid Slug Flow in a Horizontal Pipe: Experiments and Simulations. *J. Fluids Struct.* **2020**, *97*, 103083. [CrossRef]
15. Khan, U.; Pao, W.; Sallih, N. A Review: Factors Affecting Internal Two-Phase Flow-Induced Vibrations. *Appl. Sci.* **2022**, *12*, 8406. [CrossRef]
16. Miwa, S.; Hibiki, T.; Mori, M. Analysis of flow-induced vibration due to stratified wavy two-phase flow. *J. Fluids Eng.* **2016**, *138*, 091302. [CrossRef]
17. Liang, Z.; Guo, C.; Wang, C. The Connection between Flow Pattern Evolution and Vibration in 90-Degree Pipeline: Bidirectional Fluid-Structure Interaction. *Energy Sci. Eng.* **2022**, *10*, 308–323. [CrossRef]
18. Laurent, D.M.; Joris, D. A Study of the Vibration of a Horizontal U-Bend Subjected to an Internal Upwards Flowing Air-Water Mixture. *J. Fluids Struct.* **2020**, *93*, 102883. [CrossRef]
19. Elyyan, M.A.; Perng, Y.Y.; Doan, M. Fluid-Structure Interaction Modeling of a Subsea Jumper Pipe. In Proceedings of the International Conference on Offshore Mechanics and Arctic Engineering, San Diego, CA, USA, 8–13 June 2014. [CrossRef]
20. Li, F.Q.; Cao, J.; Duan, M.L.; An, C.; Su, J. Two-phase flow induced vibration of subsea span pipeline. In Proceedings of the 26th International Ocean and Polar Engineering Conference, Rhodes, Greece, 26 June–1 July 2016.
21. Zhu, H.; Gao, Y.; Hu, J.; Zhao, H.; Bao, Y. Temporal-spatial mode competition in slug-flow induced vibration of catenary flexible riser in both in plane and out of plane. *Appl. Ocean. Res.* **2022**, *119*, 103017. [CrossRef]
22. Heijden, B.; Smienk, H.; Metrikine, A.V. Fatigue analysis of subsea jumpers due to slug flow. In Proceedings of the International Conference on Offshore Mechanics and Arctic Engineering, American Society of Mechanical Engineers, San Francisco, CA, USA, 8–13 June 2014. [CrossRef]
23. Jia, D. Effect of boundary conditions, flow rate, slug length, and slug frequency on slug flow induced vibration in a pipeline span. In Proceedings of the 2013 Offshore Technology Conference, Houston, TX, USA, 6–9 May 2013.
24. Chica, L.; Pascali, R.; Jukes, P.; Ozturk, B.; Gamino, M.; Smith, K. Detailed FSI analysis methodology for subsea piping components. In Proceedings of the 31st International Conference on Ocean, Offshore and Arctic Engineering, Rio de Janeiro, Brazil, 1–6 July 2012.
25. Staurland, G.; Aamodt, M. Designing Offshore Pipeline Systems Divided into Sections of Different Design Pressures. In Proceedings of the 2004 International Pipeline Conference, Calgary, AB, Canada, 4–8 October 2004. [CrossRef]
26. Mansour, M.; Landage, A.; Khot, P.; Nigam, K.D.; Janiga, G.; Thévenin, D.; Zahringer, K. Numerical study of gas-liquid two-phase flow regimes for upward flow in a helical pipe. *Ind. Eng. Chem. Res.* **2019**, *59*, 3873–3886. [CrossRef]
27. Huang, X.; Zhang, L.H.; Zhang, R.H.; Chen, X.Z.; Zhao, Y.L.; Yuan, S. Numerical simulation of gas-liquid two-phase flow in the micro-fracture networks in fractured reservoirs. *J. Nat. Gas. Sci. Eng.* **2021**, *94*, 104101. [CrossRef]
28. Zahedi, R.; Rad, A.B. Numerical and experimental simulation of gas-liquid two-phase flow in 90-degree bend. *Alex. Eng. J.* **2022**, *61*, 2536–2550. [CrossRef]
29. Tanaka, N. Numerical Investigation of 3D Flow Properties around Finite Emergent Vegetation by Using the Two-Phase Volume of Fluid (VOF) Modeling Technique. *Fluids* **2022**, *7*, 175. [CrossRef]
30. Hirt, C.W.; Nichols, B.D. Volume of Fluid (VOF) method for the dynamics of free boundaries. *J. Copmut. Phys.* **1981**, *39*, 201–225. [CrossRef]
31. Zuzio, D.; Orazzo, A.; Estivalèzes, J.L.; Lagrange, I. A new efficient momentum preserving Level-Set/VOF method for high density and momentum ratio incompressible two-phase flows. *J Comput. Phys.* **2020**, *410*, 109342. [CrossRef]
32. Zhang, Y.; He, C.; Li, P. Numerical investigation of gas-liquid two-phase flow in horizontal pipe with orifice plate. *Prog. Nucl. Energ.* **2021**, *138*, 103801. [CrossRef]
33. Sergeev, V.; Vatin, N.; Kotov, E.; Nemova, D.; Khorobrov, S. Slug Regime Transitions in a Two-Phase Flow in Horizontal Round Pipe. CFD Simulations. *Appl. Sci.* **2020**, *10*, 8739. [CrossRef]
34. Harishkumar, T.K.; Chandrakant, R.K.; Satish, B.S. Two-way Fluid-Structure Interaction Analysis of Single Pad Externally Adjustable Fluid Film Bearing. *Eng. Sci.* **2022**, *20*, 352–363.
35. Zhu, H.J.; Hu, Y.N.; Tang, T.; Ji, C.N.; Zhou, T.M. Evolution of Gas-Liquid Two-Phase Flow in an M-Shaped Jumper and the Resultant Flow-Induced Vibration Response. *Processes* **2022**, *10*, 2133. [CrossRef]
36. Orszag, S.A.; Yakhot, V.; Flannery, W.S.; Boysan, F.; Choudhury, D.; Maruzewski, J.; Patel, B. Renormalization group modeling and turbulence simulations. In Proceedings of the International Conference on Near-Wall Turbulent Flows, Tempe, AZ, USA, 15–17 March 1993.

37. Barth, T.J.; Jespersen, D. The design and application of upwind schemes on unstructured meshes. In Proceedings of the 27th Aerospace Sciences Meeting, Reno, NV, USA, 9–12 January 1989. [CrossRef]

38. Dhande, D.Y.; Pande, D.W. A two-way FSI analysis of multiphase flow in hydrodynamic journal bearing with cavitation. *J. Braz. Soc. Mech. Sci.* **2017**, *39*, 3399–3412. [CrossRef]

39. Negrut, D.; Rampalli, R.; Ottarsson, G.; Sajdak, A. On the Use of the HHT Method in the Context of Index 3 Differential Algebraic Equations of Multibody Dynamics. In Proceedings of the ASME 2005 International Design Engineering Technical Conferences and Computers and Information in Engineering Conference, Long Beach, CA, USA, 24–28 September 2005; pp. 207–218. [CrossRef]

40. Bamidele, O.E.; Ahmed, W.H.; Hassan, M. Characterizing two-phase flow-induced vibration in piping structures with U-bends. *Int. J. Multiph. Flow.* **2022**, *151*, 104042. [CrossRef]

41. Shadloo, M.S.; Rahmat, A.; Karimipour, A.; Wongwises, S. Estimation of pressure drop of two-phase flow in horizontal long pipes using artificial neural networks. *J. Energ. Resour.* **2020**, *142*, 112110. [CrossRef]

42. Wang, Z.W.; He, Y.; Li, M.Z.; Qiu, M.; Huang, C.; Liu, Y.D.; Wang, Z. Fluid-Structure Interaction of Two-Phase Flow Passing Through 90° Pipe Bend Under Slug Pattern Conditions. *China Ocean. Eng.* **2021**, *35*, 914–923. [CrossRef]

43. Fu, B.W.; Wan, D.C. Numerical study of vibrations of a vertical tension riser excited at the top end. *J. Ocean. Eng. Sci.* **2017**, *2*, 268–278. [CrossRef]